Developments in the Built Environment 24 (2025) 100771

Contents lists available at ScienceDirect

Developments in the Built Environment

journal homepage: www.sciencedirect.com/journal/developments-in-the-built-environment

Deployability, mechanical response, and energy harvesting capacity of a novel solar roof for sports stadiums

Rana Nazifi Charandabi [a], Julia de Castro Motta [b], Gerardo Carpentieri [b], Enrico Babilio [c], Jordi Bonada [d,1], Nicholas Fantuzzi [e], Fernando Fraternali [b,*]

[a] Department of Information Engineering, Electrical Engineering and Applied Mathematics, University of Salerno, Fisciano (SA), Italy
[b] Department of Civil Engineering, University of Salerno, Fisciano (SA), Italy
[c] Department of Structures for Engineering and Architecture (DiSt), University of Naples 'Federico II', Italy
[d] Department of Strength of Materials and Structural Engineering, Universitat Politècnica de Catalunya, Barcelona, Spain
[e] Department of Civil, Chemical, Environmental and Materials Engineering, University of Bologna, Italy

ARTICLE INFO

Keywords:
Tensegrity
Solar stadiums
PV roof
Sun-tracking
Wind forces
Vibration modes

ABSTRACT

This study investigates the mechanical behavior and solar energy harvesting capabilities of a novel deployable tensegrity roof structure integrated with sun-tracking photovoltaic systems. An advancement of a recently introduced concept in stadium architecture is proposed for the design of new solar stadiums and the retrofitting of existing ones. The presented study begins with an examination of the kinematics and mechanical performance of a modular unit that serves as the foundational element of a deployable solar roof system. Owing to its high versatility, this module can be adapted to a variety of roof configurations. The study combines analytical investigation of the system's kinematics with numerical simulations of its vibration modes and structural response under varying levels of cable pretension and wind loading. Finally, the research highlights the improved solar energy harvesting capacity of the system, made possible by the independent tilting of individual roof modules across a sports stadium.

1. Introduction

There is increasing research interest in the optimal design of photovoltaic (PV) systems equipped with sun-tracking capabilities, aiming to overcome the energy harvesting losses typically associated with fixed-tilt systems, while maintaining convenient activation costs (Lim et al., 2020; Gao et al., 2019; Pawlak-Jakubowska, 2023; Cheggaga et al., 2024). In particular, multiple-axis PV trackers can significantly boost energy production compared to fixed-tilt installations, achieving gains of up to 30%, as observed in the case of dual-axis systems (Lim et al., 2020). Nevertheless, further studies are required to better assess the trade-off between the energy gains provided by sun-tracking and key factors such as cost, durability, and long-term reliability. It has been observed that several existing designs are unable to simultaneously optimize tracking precision and mechanical robustness, although promising solutions to address these challenges have been proposed in the literature (Lim et al., 2020). For instance, sun-tracking strategies under partial shading conditions have been developed for photovoltaic greenhouses (Gao et al., 2019), while a retractable sun-tracking roof structure aimed at enhancing spatial efficiency in building environments has been investigated (Pawlak-Jakubowska, 2023). Moreover, the importance of optimizing the costs associated with sun-tracking activation strategies has been emphasized in Cheggaga et al. (2024), where a cost-effective solar tracker capable of enhancing PV efficiency by minimizing shading losses has been proposed. The role of effective daylighting strategies in complex roof structures and expansive architectural spaces has also been investigated, highlighting their potential to complement solar energy solutions in building design (Born et al., 2024; Heinzelmann, 2018). The relevant potential of solar roofs in future urban scenarios is well described in Ürge-Vorsatz et al. (2025).

A recent study analyzed the integration of tensegrity structures with sun-tracking photovoltaic systems for stadium architecture (Nazifi Charandabi et al., 2025). Although lightweight and adaptive designs have been explored separately in previous works (Tahmasebinia et al., 2023; Fraternali et al., 2024b), their application to energy-harvesting stadium roofs remains limited. The research presented in Nazifi Charandabi et al. (2025) advances the field by introducing a modular tensegrity roof, optimized for minimal mass, that combines structural stability with efficient solar energy production through innovative sun-tracking strategies (see also Babilio (2025) and Bellini (2025)). The deployment

* Corresponding author.
E-mail address: f.fraternali@unisa.it (F. Fraternali).
[1] Serra Húnter Fellow.

https://doi.org/10.1016/j.dibe.2025.100771
Received 14 August 2025; Received in revised form 1 October 2025; Accepted 2 October 2025
Available online 7 October 2025

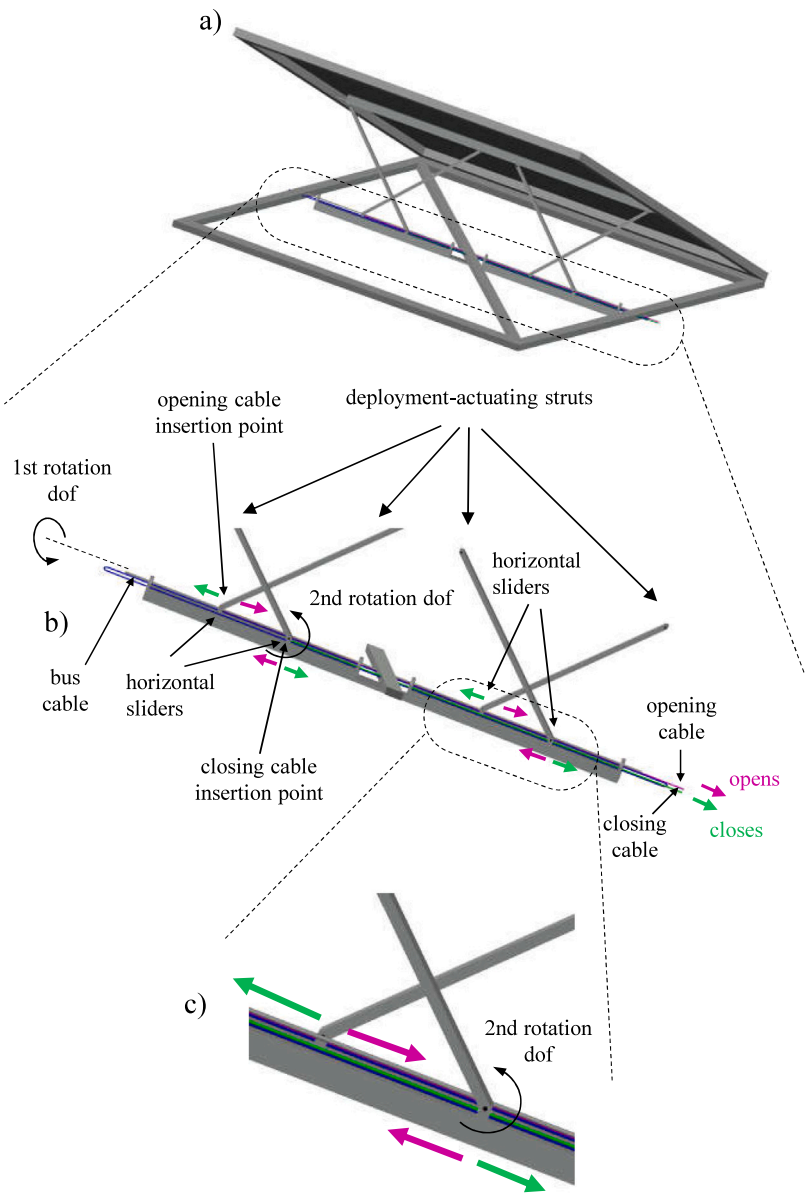

Fig. 1. Illustration of a modular element forming the scissor tensegrity roof structure: (a) tilted configuration; (b) tilting mechanism; (c) close-up view of the struts that guide the deployment mechanism. The opening cable is shown in purple, while the closing cable is shown in green.

method employed in that study uses a winch mechanism requiring minimal energy input, as demonstrated in Fraternali et al. (2024a). The present work builds substantially on that previous research by examining the kinematics, mechanical response under wind loading, and energy harvesting potential of a novel deployable solar roof structure. An innovative roof module (or unit) equipped with sun-tracking PV systems is presented. Thanks to a deployment strategy that utilizes activation struts mounted on sliding supports (see Section 2), the module can be easily integrated into existing roof structures. While previous work examined the mechanical behavior of a tensegrity structure for a solar stadium roof in its undeployed configuration, the present study investigates its performance in the deployed state, with particular attention to its response to wind-induced forces and vibration modes. An analytical study of the kinematics of this tensegrity system is presented in Section 3, while its mechanical response to wind forces and its vibration modes under different levels of cable pretension are analyzed in Sections 4–5. The solar energy harvesting capacity of the proposed roof system is examined in Section 6, through a generalization of the approach presented in Nazifi Charandabi et al. (2025), which accounts for varying tilting angles across individual roof modules. The work concludes with final remarks and directions for future research in Section 7.

2. Illustration of the deployable roof structure

Fig. 1 illustrates a modular component that constitutes the deployable structure analyzed in this study, hereafter referred to as a scissor-tensegrity. In this system, the deployment of the upper roof panels is accomplished through the actuation of four struts located beneath the panels. The upper ends of the struts are hinged at four fixed points on the deployable roof, interconnected by a longitudinal beam. The lower ends are instead attached to horizontal sliders mounted on a second longitudinal beam, which are driven by a looped bus cable. In contrast to the scissor-tensegrity system investigated in Fraternali et al. (2024b), where the bus cable was allowed to deform out of plane, the structure analyzed in this study adopts a different configuration: the bus cable is supported by rollers that move along a track beam anchored to the lower roof structure.

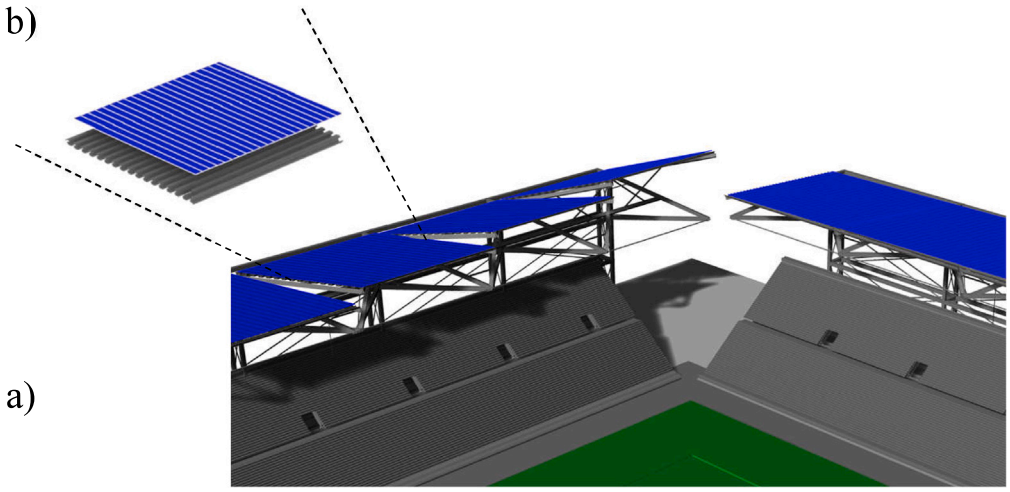

Fig. 2. (a) Application of the deployable roof system proposed in this study to the stadium structure analyzed in Nazifi Charandabi et al. (2025); (b) exploded schematic view of a corrugated metal roof panel covered with PV strips.

As shown in Fig. 1, the bus cable is connected to both an opening cable and a closing cable, which are wound around an external winch. This arrangement enables the bus cable to move continuously along the guiding track when the winch is operated. By winding the opening or closing cable around the winch, the deployment-actuating struts are raised or lowered, respectively, until reaching their maximum tilt angle (see Section 3). The motion of two adjacent pairs of actuating struts is synchronized by employing the same opening and closing cables for both (Fig. 1). The lower and upper longitudinal beams connected to the scissor struts can rotate about their own axes (first rotational degree of freedom, '1st rotation dof' in Fig. 1). At the same time, cylindrical hinges at the strut ends allow rotation about an axis orthogonal to the plane defined by the current strut configuration (second rotational degree of freedom, '2nd rotation dof'). This articulated arrangement provides a technically robust solution for accommodating large rotations at the strut ends. The upper longitudinal beam is connected to a linear cylindrical hinge that transfers the loads applied to the roof panel directly to the beam. Once the desired tilted configuration is achieved, the prestressed bus cable is secured by locking the winch mechanism. This enables the tensegrity system, comprising the cable and the deployment-actuating (or 'scissor') struts, to elastically resist external loads (cf. Sections 4 and 5).

The case of a lower roof module supported by a steel frame is shown in Fig. 1. As previously noted, this supporting structure can be substituted with any other suitable roofing system. Fig. 2 shows the application of the deployable roof modules examined in this study to the stadium structure analyzed in Nazifi Charandabi et al. (2025). Each module consists of SunBender SB 47 PV strips by Solbian (2025) mounted on metal roofing panels. The adopted strips are semiflexible photovoltaic laminates based on Maxeon Gen III solar cells. These high-performance cells are renowned for their durability and high power conversion efficiency, assumed here to be 24% in accordance with the manufacturer's specifications (Solbian, 2025). The flexibility of the laminates enables their integration into curved or movable roof structures without compromising energy performance, making them particularly suitable for deployable systems such as those examined in this study (see Section 4). The corrugated metal panels run in the longitudinal direction, while the PV strips are arranged transversely (Fig. 2b). An alternative stadium architecture, designed to allow flexible integration of the roof modules examined in this study, is presented in Section 6. Throughout the paper, the PV panels are often depicted in blue for illustrative purposes.

The following section provides an analytical treatment of a simplified kinematic model of the deployable roof panel, which, in particular, assumes that the bus cable lies along a single straight line. This model offers a reasonably accurate approximation when the two segments forming the bus cable are sufficiently close to one another. Its extension to the actual geometry shown in Fig. 1 is left to future work, which will include the fabrication of a reduced-scale physical mock-up of the deployable roof module.

3. Kinematics

We now focus on the kinematics of the basic module of the deployable roof structure, adopting the notation presented in Fig. 3 and relying on the simplifying assumptions introduced at the end of the previous section. The following formulation extends the analysis presented in Fraternali et al. (2024b) to the case of an arbitrary planar module.

We define the motion of this element as being governed by the displacement λ of node 5 along the edge 4–5, measured from the closed configuration where $\hat{\theta} = 0°$ (Fig. 4), which we assume to be the control variable (Fig. 5). Due to symmetry, an identical displacement is exhibited by node 7, while nodes 4 and 6 exhibit displacements of equal magnitude but opposite sign. It is worth noting that λ represents the change in the rest length of either the opening or closing cable that induce the tilting of the roof panels (Fig. 1). The deployable roof module can be superimposed on a supporting roof structure with an arbitrary initial (or primary) tilting angle θ_0 about the frontal edge. Fig. 4 shows a sequence of configurations corresponding to increasing secondary tilting angles, $\hat{\theta}$, measured with respect to the posterior edge of the system. The name 'scissor-tensegrity' derives from the observation that the struts of the tensegrity structure under examination exhibit a scissor-like shape for values of $\hat{\theta}$ that are sufficiently lower than its maximum value (Fig. 4).

We introduce the Cartesian frame x, y, z illustrated in Fig. 3 and use the symbol $\boldsymbol{x}_i$ to denote the position vector of node i in the reference configuration for $\hat{\theta} = 0°$, and $\boldsymbol{y}_i$ to denote the position vector of the same node in the current tilted configuration with $\hat{\theta} \neq 0°$. These positions let us to write

$$\boldsymbol{y}_4 = \boldsymbol{x}_4 - \lambda \boldsymbol{e}_x, \quad \boldsymbol{y}_5 = \boldsymbol{x}_5 + \lambda \boldsymbol{e}_x, \quad \boldsymbol{y}_6 = \boldsymbol{x}_6 - \lambda \boldsymbol{e}_x, \quad \boldsymbol{y}_7 = \boldsymbol{x}_7 + \lambda \boldsymbol{e}_x, \tag{1}$$

and

$$\boldsymbol{x}_4 = \boldsymbol{x}_5 + \ell \boldsymbol{e}_x, \quad \boldsymbol{x}_6 = \boldsymbol{x}_7 + \ell \boldsymbol{e}_x, \tag{2}$$

where ℓ denotes the fixed length of the struts 4-5′, 5-4′, 6-7′, 7-6′, and $\boldsymbol{e}_x = \{1, 0, 0\}$ is the unit vector along the x-axis. Our current goal is to express the rigid-body motion of the roof panels, which consists of a

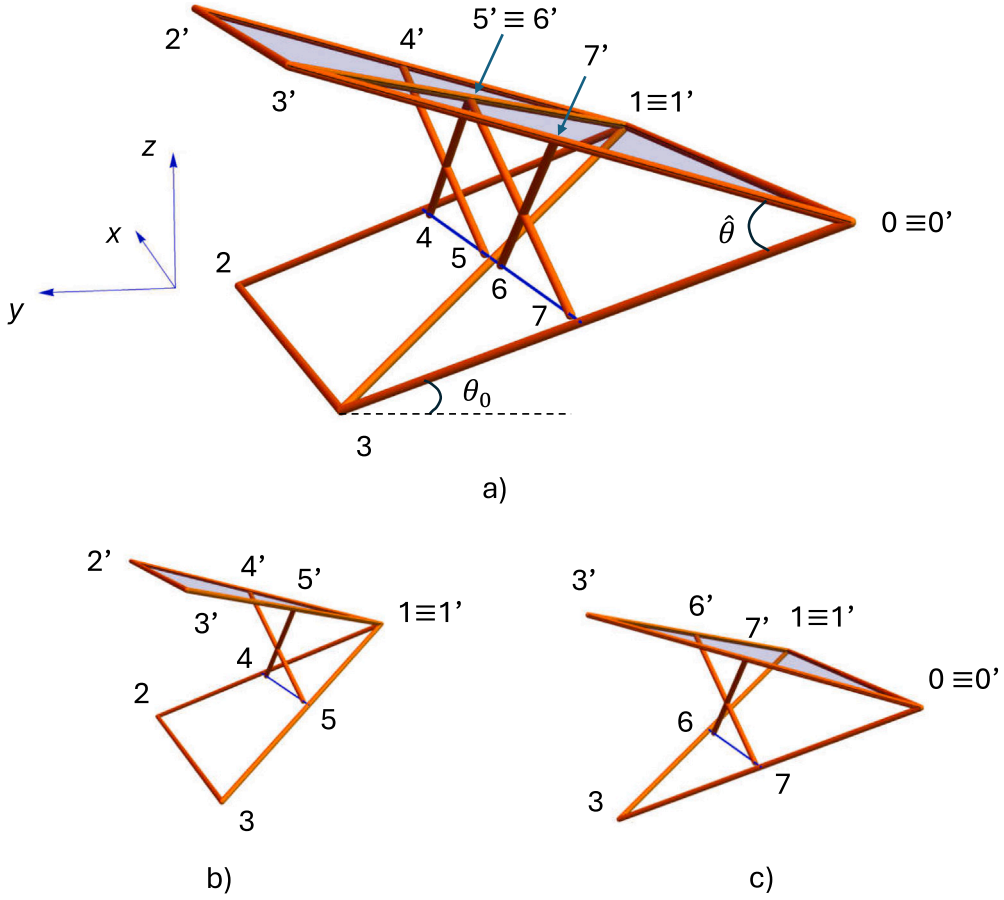

Fig. 3. (a) Notation used for the nodes of the basic module of the scissor tensegrity roof structure; (b,c) triangular elements forming such a module.

finite rotation by an angle $\hat{\theta}$ about the 0–1 edge, in terms of the control parameter λ.

Let Π denote the plane in which the roof panels lie when $\hat{\theta} = 0°$, and let Π' denote the plane in which the same panels lie in the tilted configuration. We use the notation $\mathcal{A}$ to denote the rotation axis 0–1, and $\mathcal{B}$ to denote the axis of the bus cable connecting the nodes 4, 5, 6 and 7 (Fig. 5). It is easily verified that the component of the position vector along $\boldsymbol{e}_x$ for any point lying on the tilted plane Π' remains unchanged during the rotation under examination. We can therefore write

$$\boldsymbol{y}_{4'} \cdot \boldsymbol{e}_x = \boldsymbol{x}_4 \cdot \boldsymbol{e}_x, \tag{3}$$

and similar relations for the couples of nodes 5-5′, 6-6′ and 7-7′.

We also observe that the nodes $\boldsymbol{x}_4$ and $\boldsymbol{y}_{4'}$ are at the same distance c from the $\mathcal{A}$ axis, which is given by

$$c = \|(\boldsymbol{x}_4 - \boldsymbol{x}_0) \times \boldsymbol{e}_x\| = \|(\boldsymbol{y}_{4'} - \boldsymbol{x}_0) \times \boldsymbol{e}_x\|. \tag{4}$$

Let $\bar{0}$, $\bar{1}$, $\bar{2} \equiv 2$ and $\bar{3} \equiv 3$ denote the orthogonal projections of nodes 0, 1, 2 and 3 onto the horizontal plane passing through the nodes 2 and 3, respectively. If we assume that the edges $\bar{1}-\bar{2}$, $\bar{1}-\bar{3}$, and $\bar{0}-\bar{3}$ have length r; that the edges $\bar{1}-\bar{2}$ and $\bar{1}-\bar{3}$, as well the edges $\bar{1}-\bar{3}$ and $\bar{0}-\bar{3}$ form an angle α; that the height of nodes 0 and 1 above the horizontal plane is h; and that the bus cable connects the midpoints of edges 1–2, 1–3, and 0–3, we can write

$$c = \frac{1}{2}\sqrt{h^2 + \left(r\cos\left(\frac{\alpha}{2}\right)\right)^2}, \quad L = 2r\sin\left(\frac{\alpha}{2}\right), \quad \ell = \frac{L}{2}, \tag{5}$$

with L denoting the length of the 2–3 edge.

We now introduce the distance $s = s(\lambda)$ between nodes 4 and 5 in the current (tilted) configuration of the deployable roof module, which can be readily computed as follows

$$s = (\boldsymbol{y}_{4'} - \boldsymbol{y}_5) \cdot \boldsymbol{e}_x = (\boldsymbol{x}_4 - \boldsymbol{y}_5) \cdot \boldsymbol{e}_x = \ell - \lambda. \tag{6}$$

On the other hand, let $\eta = \eta(\lambda)$ be the perpendicular distance from $\boldsymbol{y}_{4'}$ to the axis $\mathcal{B}$. From the Pythagorean theorem, we obtain (see Fig. 5)

$$\eta^2 = \ell^2 - s^2 = 2\lambda\ell - \lambda^2. \tag{7}$$

We can now relate the tilting angle $\hat{\theta}$ to the control variable λ by examining the isosceles triangle with legs c and hypotenuse η, as shown in Fig. 5. Applying the law of cosines to this triangle, we obtain

$$\eta^2 = 2c^2 - 2c^2\cos(\hat{\theta}), \tag{8}$$

from which we deduce

$$\hat{\theta} = \arccos\left(1 - \frac{\eta^2}{2c^2}\right) = \arccos\left(1 - \frac{2\lambda\ell - \lambda^2}{2c^2}\right). \tag{9}$$

The maximum value of η is attained when $s = 0$, i.e., $\eta_{max} = \ell$. The corresponding maximum tilting angle is then given by

$$\hat{\theta}_{max} = \arccos\left(1 - \frac{\ell^2}{2c^2}\right). \tag{10}$$

It is easily verified that $\hat{\theta}_{max} = 119°$ when $r = 12$ m, $h = 5$ m and $\alpha = \pi/2$, as in the structure analyzed in Nazifi Charandabi et al. (2025).

The positions of the nodes of the roof panels in the tilted configuration are computed through

$$\boldsymbol{y}_{i'} = \mathbf{R}_x(\theta)(\boldsymbol{x}_{i'} - \boldsymbol{x}_0) + \boldsymbol{x}_0, \tag{11}$$

where $\mathbf{R}_x(\hat{\theta})$ is the matrix representing a rotation about the x-axis, defined as follows

$$\mathbf{R}_x(\hat{\theta}) = \begin{bmatrix} 1 & 0 & 0 \\ 0 & \cos\hat{\theta} & -\sin\hat{\theta} \\ 0 & \sin\hat{\theta} & \cos\hat{\theta} \end{bmatrix}. \tag{12}$$

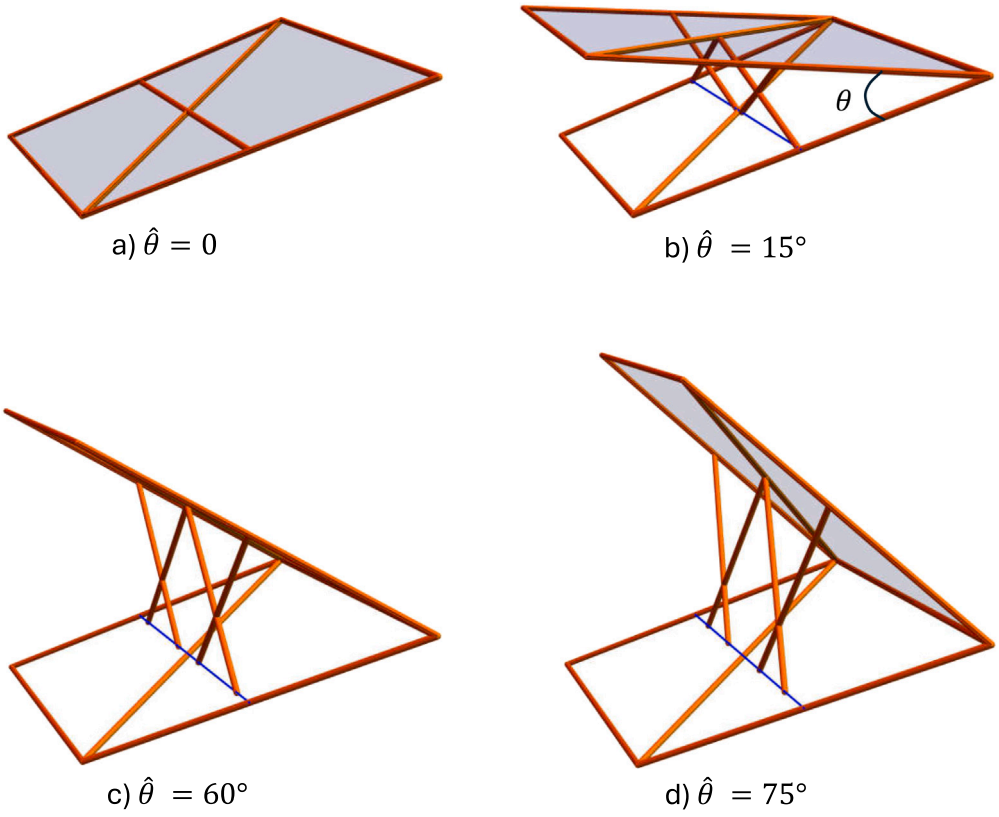

Fig. 4. Sequence showing various configurations of the roof element corresponding to different tilting angles $\hat{\theta}$.

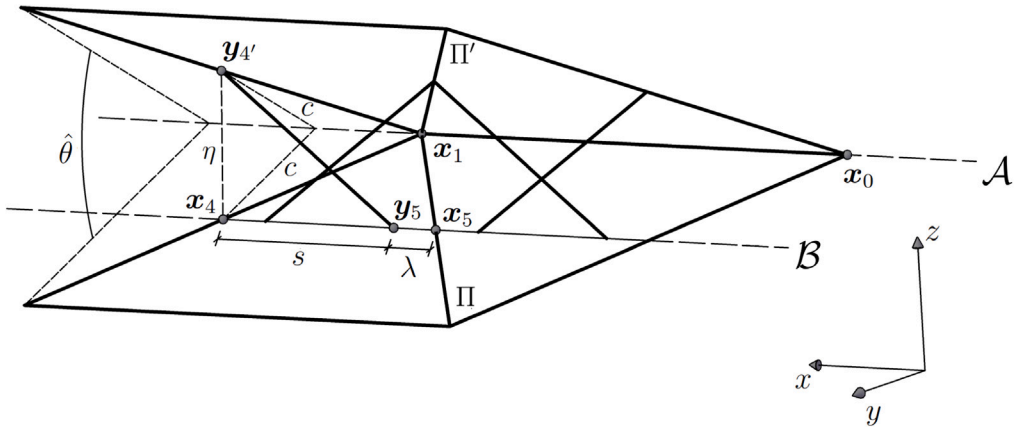

Fig. 5. Illustration of the parameters governing the kinematics of the deployable roof module.

Finally, the unit normal to the tilted configuration of the roof panels is given by

$$\boldsymbol{n}(\lambda) = \frac{(\boldsymbol{y}_{4'} - \boldsymbol{x}_1) \times (\boldsymbol{x}_1 - \boldsymbol{x}_0)}{\|(\boldsymbol{y}_{4'} - \boldsymbol{x}_1) \times (\boldsymbol{x}_1 - \boldsymbol{x}_0)\|}. \tag{13}$$

The kinematic analysis presented above shows that the secondary tilting angle $\hat{\theta}$ ranges from 0° in the closed ('fully folded') configuration to the maximum value given by Eqn. (10), which equals 119° in the benchmark example studied in Nazifi Charandabi et al. (2025). In the closed configuration ($\hat{\theta} = 0$, see Fig. 4a), the scissor struts lie horizontally. This condition demands the highest power input from the actuation system, as the struts must be lifted into a slightly inclined configuration against the weight of the roof panel. Nevertheless, the overall energy demand of the system remains low compared to the electric motors typically used for tilting PV panels. This efficiency stems from the winch-based mechanism, which only requires adjusting the rest length of the bus cable. The low energy consumption of this system has been experimentally validated in Fraternali et al. (2024b).

4. Mechanical response to wind loads

This section illustrates the mechanical response of a physical prototype of the deployable roof module, superimposed on a base steel frame structure. The latter consists of triangular cells, as depicted in the simplified finite element model in Fig. 6. We define the base cells as isosceles triangles, with the two transverse edges measuring 13 m and the longitudinal edge measuring 16.97 m (dimensions refer to the centerlines of the steel members). The rear node is elevated by 5 m with respect to the nodes on the longitudinal edge, resulting in an initial tilting angle about the frontal edge of $\theta_0 = 0.532\,\text{rad} = 30.509°$ (see Fig. 3). Although not explicitly shown in the subsequent

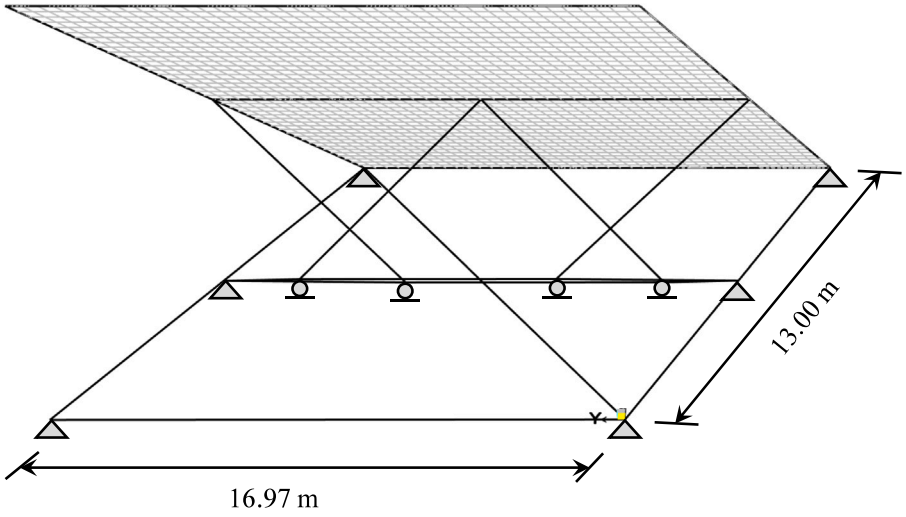

Fig. 6. Finite element model of a physical prototype of the deployable roof unit.

figures, the structural role of the lower longitudinal beam described in Section 2 (see Fig. 1) is represented in the model through roller supports at the lower ends of the scissor struts. This beam is assumed to be sufficiently stiff, so that vertical displacements at the roller supports can be neglected.

The main steel members are fabricated from square hollow sections (SHS) with an edge length of 400 mm and a wall thickness of 16 mm. In contrast, the scissor struts are made from steel SHS profiles with an edge length of 180 mm and the same wall thickness (see Fondazione Promozione Acciaio, 2024). All profiles used belong to ductility class 1, as defined in the Italian standard NTC (2018). Members exceeding 12 m in length can be assembled by joining together shorter segments, in accordance with Eurocode 3 (European Committee for Standardization (CEN), 2024), or alternatively transported as single units from the manufacturing plant to the construction site using specialized vehicles, as permitted, e.g., by European Directive 96/53/EC. In the following analysis, we examine two alternative solutions for the bus cable, utilizing spiral strand steel wire ropes supplied by Sirtef srl (2025), with diameters of either 57 mm or 66 mm. As anticipated in Section 2, we assume that the deployable roof panels consist of longitudinally oriented corrugated steel elements, with lightweight PV panel strips applied on top in an orthogonal arrangement (see Fig. 2b).

A finite element simulation of the elastic response of the deployable roof model to wind loading was carried out using SAP2000® (Computers and Structures, Inc., 2016), considering configurations with different tilting angles and assuming that the deployment mechanism is locked. The finite element model (FEM) shown in Fig. 6 consists of 14 bars, 6 cables, 1600 quadrilateral shell elements, and 1689 joints. We assume that all bars and cables are made of steel with a mass density of $7862\,\mathrm{kg\,m^{-3}}$. For the bars, the material properties include a Young's modulus of $E_b = 206\times10^9\,\mathrm{N\,m^{-2}}$ and a yield stress $\sigma_Y = 223\times10^6\,\mathrm{N\,m^{-2}}$. For the cables, the Young's modulus is $E_s = 160\times10^9\,\mathrm{N\,m^{-2}}$ and the yield stress is $\sigma_Y = 1200\times10^6\,\mathrm{N\,m^{-2}}$, as specified by the manufacturer of the spiral strand steel wire ropes (Sirtef srl, 2025). The manufacturer also declares maximum breaking forces (MBF) of 2610 kN and 3490 kN for the 57 mm and 66 mm cables, respectively. The shell elements exhibit membrane and bending properties consistent with those of the metal roofing panels used in the deployable roof structure. These elements have a height of 220 mm, a thickness of 4 mm, and a self-weight of $486\,\mathrm{N\,m^{-2}}$. They are assumed to be made of the same steel as the bars and support PV panels with a self-weight of $44\,\mathrm{N\,m^{-2}}$, including a wire mesh backing (see Nazifi Charandabi et al., 2025 for more details). The boundary conditions of the FEM include roller supports at the lower ends of the scissor struts, hinged supports at all other lower nodes (see Fig. 6), and internal hinges at the beam connections.

Table 1
Load factors for the analyzed load combinations at the ultimate limit state: G denotes the dead loads, P the prestress forces, W_d the downward wind forces, and W_u the upward wind forces.

Ultimate limit state	Load combination
DULS	$1.3G + P$
WULS_d	$1.3G + 1.5W_d + P$
WULS_u	$1.0G + 1.5W_u + P$

We analyzed load cases comprising dead loads, cable pretension, and wind forces, using an equivalent static force approach to represent the effects of both downward and upward (lifting) wind actions. These load cases account for the combined action of positive wind pressures (acting toward the roof module) and negative wind pressures (acting away from the roof module) on the two faces of the deployable roof panel, corresponding to downward and upward wind forces. The ultimate limit state (ULS) analysis of the roof module was carried out using the load combinations defined by NTC (2018), as presented in Table 1. This table introduces the symbols G, P, and W to represent the load conditions corresponding to dead loads (including the self-weight of the structure, the weight of the roof panels, and the PV strips), cable pretension forces, and wind actions, respectively.

The load combinations listed in Table 1 include one that accounts for dead loads and prestress forces (DULS), along with two additional combinations that include dead loads, prestress forces, and wind actions, corresponding to either downward (W_d) or upward (W_u) forces (WULS_d and WULS_u combinations, respectively). It is worth noting that the WULS combinations consistently proved to be more critical than the DULS combinations in all the analyses and verifications presented below. The design values for wind loading were specified in accordance with the Italian structural code NTC (2018). The site coordinates of the city of Salerno were used: Latitude: 40°40′31.62″N and Longitude: 14°47′35.81″E. The wind pressure was defined as the net value obtained from the vector sum of the positive and negative external pressures estimated to act on the two faces of the roof module (NTC, 2018). This approach was applied to both downward and upward wind loading in the examined configurations. The wind dynamic factor was set equal to unity, based on the assumption that significant dynamic effects may be neglected in a preliminary assessment (see Section 5). Future work will focus on refining the current simplified wind loading model through wind tunnel tests on reduced-scale mockups of the deployable roof module (both isolated and in array), accounting for the effects of varying wind directions and tilt angles (Wittwer et al., 2022). The mechanical response of the FEM was predicted using the nonlinear static

Table 2
Maximum cable forces for the $WULS_d$ combination, along with the corresponding ratios between the maximum breaking force of the employed bus cable and the maximum cable forces. The results are presented for $\hat{\theta} = 30°$, 45°, and 75°, considering different diameters of the bus cable and various pretension levels τ.

$\hat{\theta}$ [deg]	τ [%]	MCF [kN]		MBF/MCF	
		$d = 57$ mm	$d = 66$ mm	$d = 57$ mm	$d = 66$ mm
30	0	1055.324	1048.598	2.473	3.328
	25	1012.081	1205.408	2.579	2.895
	40	1357.576	1717.159	1.923	2.032
	50	1612.067	2058.321	1.619	1.696
45	0	672.965	674.959	3.878	5.171
	25	904.570	1125.823	2.885	3.100
	40	1286.609	1637.921	2.029	2.131
	50	1541.300	1979.317	1.693	1.763
75	0	339.168	342.250	7.695	10.197
	25	813.462	1031.511	3.209	3.383
	40	1195.632	1543.781	2.183	2.261
	50	1450.412	1885.294	1.799	1.851

Table 3
Maximum cable forces for the upward wind combination $WULS_u$, considering different diameters of the bus cable and different pretension levels τ.

$\hat{\theta}$ [deg]	τ [%]	MCF [kN]		MBF/MCF	
		$d = 57$ mm	$d = 66$ mm	$d = 57$ mm	$d = 66$ mm
30	0	83.772	84.840	31.156	41.136
	25	737.695	964.112	3.538	3.620
	40	1134.183	1495.592	2.301	2.334
	50	1398.501	1849.909	1.866	1.887
45	0	69.127	71.186	37.757	49.026
	25	703.909	924.593	3.708	3.775
	40	108.871	1440.597	23.973	2.423
	50	1345.505	1784.607	1.940	1.956
75	0	87.342	90.027	29.883	38.766
	25	695.205	904.701	3.754	3.858
	40	1077.689	1427.391	2.422	2.445
	50	1332.678	1769.184	1.958	1.973

analysis option in SAP2000®, accounting for material nonlinearities due to the tension-only response of the cables and large displacement effects. Configurations of the deployable roof module corresponding to various tilting angles are examined, making use of the kinematic model presented in Section 3, with the aim of investigating the influence of this parameter on the mechanical response of the system. The analysis focuses on the displacements of the roof panels and the forces carried by the bus cable and the scissor struts. The response of the base supporting structure lies beyond the scope of this study; relevant findings on this topic are presented in Nazifi Charandabi et al. (2025).

Tables 2 and 3 present the results for the maximum bus cable forces (MCF) obtained under the $WULS_{d,u}$ load combinations (see Fig. 6). The analysis was carried out for $\hat{\theta} = 30°$, 45°, and 75°, considering various bus cable diameters and cable pretension levels τ, expressed as percentages of the maximum breaking force (MBF). The results demonstrate the attainment of satisfactory safety factors with respect to cable forces at the ultimate limit state (ULS), as the MBF/MCF ratios are consistently greater than one. The results for the $WULS_u$ combination show that the MBF/MCF ratio is approximately equal to the applied pretension level when $\tau \neq 0$. In the absence of cable pretension, however, this ratio reaches high values (e.g., nearly 49 for $\hat{\theta} = 45°$ and $d = 66$ mm), corresponding to low MCF/MBF ratios (see Table 3). This behavior arises because dead loads and upward wind forces tend to induce axial forces of opposite sign in the bus cable, leading to relatively low total cable forces under the $WULS_u$ combination when $\tau = 0$

Table 4 presents the results of the safety check for the scissor struts, carried out for the $WULS_d$ combination, which proved to be the most critical among those listed in Table 1. It can be readily verified that the design compressive resistance $N_{c,Rd}$ of these elements, calculated according to NTC (2018), is 2103.810 kN, while the Euler buckling load N_{cr}, based on the member geometry and the assumed mechanical properties of the material, is 1065.139 kN. Let N_{Ed} denote the maximum compressive design force (in absolute value) acting on these elements, for a given tilting angle $\hat{\theta}$ and a specified level of pretension in the bus cable (hereafter also referred to as the prestress level of the system). Since the Euler buckling load of the struts is about 50% lower than their compressive design strength, a simplified safety assessment is performed by evaluating the ratio N_{Ed}/N_{cr}, as reported in Table 4. The results in the table show that the N_{cr}/N_{Ed} ratio remains consistently greater than one across all examined roof module configurations, particularly when the cable pretension is nonzero, as expected in a properly designed tensegrity system. The highest buckling load safety factors are observed at higher levels of bus cable pretension, and the N_{cr}/N_{Ed} ratio varies only marginally when the pretension increases from $\tau = 20\%$ MBF to $\tau = 50\%$ MBF.

Table 4
Maximum compressive forces N_{Ed} in the scissor struts for the $WULS_d$ combination, along with the corresponding ratios between the Euler buckling load (N_{cr} = 1065.139 kN) and the maximum strut forces. The results are provided for $\hat{\theta} = 30°$, 45°, and 75°, considering different bus cable diameters and prestress levels.

$\hat{\theta}$ [deg]	τ [%]	$d = 57$ mm		$d = 66$ mm	
		N_{Ed} [kN]	N_{cr}/N_{Ed}	N_{Ed} [kN]	N_{cr}/N_{Ed}
30	0	880.977	1.2090	855.603	1.2449
	25	659.362	1.6154	682.075	1.5616
	40	654.837	1.6266	681.929	1.5619
	50	654.703	1.6269	681.821	1.5622
45	0	583.039	1.8269	575.341	1.8513
	25	513.632	2.0737	523.004	2.0366
	40	513.603	2.0739	522.976	2.0367
	50	513.581	2.0739	522.953	2.0368
75	0	361.775	2.9442	360.180	2.9572
	25	349.674	3.0461	351.244	3.0325
	40	349.667	3.0462	351.238	3.0325
	50	349.663	3.0462	351.234	3.0326

Fig. 7 graphically illustrates the deformed shapes obtained for the $WULS_d$ (Fig. 7a–c) and $WULS_u$ combinations (Fig. 7d–f), corresponding to tilting angles $\hat{\theta} = 30°$ (panels a,d), 45° (panels b,e), and 75° (panels c,f). These results were computed for a prestress level of $\tau = 40\%$ MBF and a bus cable diameter of $d = 57$ mm. Table 5 reports the minimum and maximum tip deflections, $v_{tip,\min}$ and $v_{tip,\max}$, defined as the minimum and maximum norms of the displacement vectors of the frontal-edge nodes.

The results shown in Fig. 7 and Table 5 indicate that the maximum deflections occur in the roof panel with $\hat{\theta} = 30°$ and that such deflections decrease by increasing the tilting angle of the panel and the pretension of the bus cable. It should be noted that the adopted SunBender SB 47 photovoltaic panels by Solbian are designed to be semiflexible and capable of withstanding significant deflections. Each panel consists of strips measuring 80 mm in width and 1054 mm in length, with a thickness of 2 mm, and incorporates Maxeon Gen III solar cells. These cells are renowned for their excellent mechanical and electrical performance even under severe environmental conditions (Solbian, 2025), as has been previously observed. The maximum tip deflection of approximately 359 mm, observed without cable pretension under downward wind loading in the panel with $\hat{\theta} = 30°$ (reduced to about 224 mm with a pretension of 40% MBF, see Table 5), occurs at the tip of a PV panel strip spanning roughly 13 m and comprising 12 panels, each 1.054 m in length. We obtained a rough estimate of the curvatures of the PV panels forming the strip by dividing the nodal rotations of the shell elements by the distances between adjacent nodes. Applying this approach to the most bent roof panel

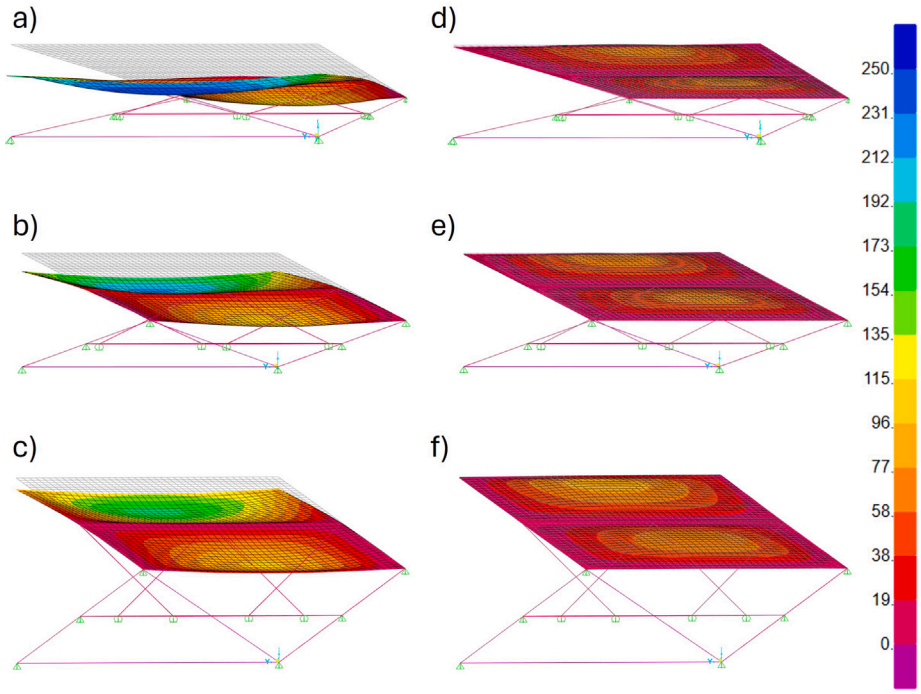

Fig. 7. Deformed shapes and color maps of the displacement vector norms (mm) under the load combinations WULS_d (a, b, c) and WULS_u (d, e, f) are shown for the deployable roof module with tilting angles $\hat{\theta} = 30°$ (a, d), 45° (b, e), and 75° (c, f), a prestress level of $\tau = 40\%$ MBF, and a bus cable diameter of $d = 57$ mm. Displacements are magnified by a factor of 10 in the deformed shape plots; no amplification is applied in the color maps. (For interpretation of the references to color in this figure legend, the reader is referred to the web version of this article.)

Table 5
Minimum and maximum norms of the displacement vectors (in mm) recorded at the tip nodes of the deployable roof modules with tilting angles $\hat{\theta} = 30°$ (a), 45° (b), and 75° (c). Different prestress levels τ [% MBF] applied to the bus cable with diameter $d = 57$ mm are analyzed. The presented values are obtained for the load combinations WULS_d (downward wind) and WULS_u (upward wind).

$\hat{\theta}$	τ [%]	WULS_d		WULS_u	
		$v_{tip,\min}$	$v_{tip,\max}$	$v_{tip,\min}$	$v_{tip,\max}$
30	0	306.605	358.678	2.919	10.829
	25	178.382	229.022	2.769	10.105
	40	172.606	223.971	2.786	10.035
	50	172.551	223.917	2.798	9.989
45	0	176.837	227.594	3.141	8.457
	25	133.342	181.158	3.102	7.189
	40	133.326	181.142	3.104	7.175
	50	133.313	181.131	3.105	7.164
75	0	99.467	142.610	9.450	21.127
	25	92.148	134.053	6.857	18.618
	40	92.147	134.051	6.858	18.620
	50	92.147	134.050	6.858	18.621

strip under the WULS_d load combination, we estimated, in the most severe case ($\hat{\theta} = 30°$ and $\tau = 0$), a maximum local curvature of approximately 0.242 m^{-1} (curvature radius 4.136 m), with an average value of 0.045 m^{-1} and a standard deviation of 0.060 m^{-1} (absolute value). These values are well within the safe limit for the semiflexible panels employed. According to the manufacturer, the panels can indeed withstand a maximum curvature of 1.00 m^{-1} (minimum curvature radius of 1 m), corresponding to a central deflection of 122 mm over an arc length of 1 m (Solbian Manual, 2025).

The deflections exhibited by the deployable roof module under upward wind forces are significantly lower than those observed under downward wind conditions, since the upward wind forces tend to counteract the deflections induced by dead loads (see panels d, e, and f of Fig. 7), as we already observed. We conclude by observing that the present displacement analysis has been carried out in the ultimate limit state (ULS), whereas technical standards require such evaluations to be performed in the serviceability limit state (SLS), which is associated with lower levels of applied forces (NTC, 2018).

5. Vibration modes

This section presents the results of a linear modal analysis of the undamped vibration modes of the deployable roof panel, performed for configurations with different tilting angles. Such a study is based on the deformed shapes obtained at the end of the nonlinear analyses under the WULS_d load combination (Fig. 8). Fig. 8 illustrates the vibration mode shapes for the first three modes of roof panels with tilting angles $\hat{\theta} = 30°$ (Figs. a–c) and $\hat{\theta} = 75°$ (Figs. d-f), assuming a prestress level of $\tau = 40\%$ MBF and a bus cable diameter of 57 mm. The plots show the mode shapes normalized with respect to the FEM mass matrix, with the colorbar indicating the variation in the norms of the nodal displacement vectors. Tables 6–8 present the fundamental periods and frequencies associated with the first three vibration modes of panels at the tilting angles mentioned above, considering various prestress levels and bus cable diameters. Results for $\tau = 50\%$ MBF are not shown, as they are nearly identical to those for $\tau = 40\%$ MBF in the present case.

The plots shown in Fig. 8 indicate that the first vibration mode of the deployable roof panel is of the bending type (similar to the deformed shapes in Fig. 7a,c), the second mode is torsional, and the third mode exhibits a coupled bending–torsional behavior. On the other hand, the results presented in Tables 6–8 show that the fundamental frequency of the first mode increases with both the tilting angle and the cable prestress level. Referring to the most significant cases with $\tau \neq 0$, we observe that the fundamental frequencies are slightly above or approximately equal to 2 Hz when the bus cable is pretensioned to 40% or more of its maximum breaking force. It is worth noting that wind loading is a dynamic action that can induce resonance-like responses in structures or structural components with fundamental

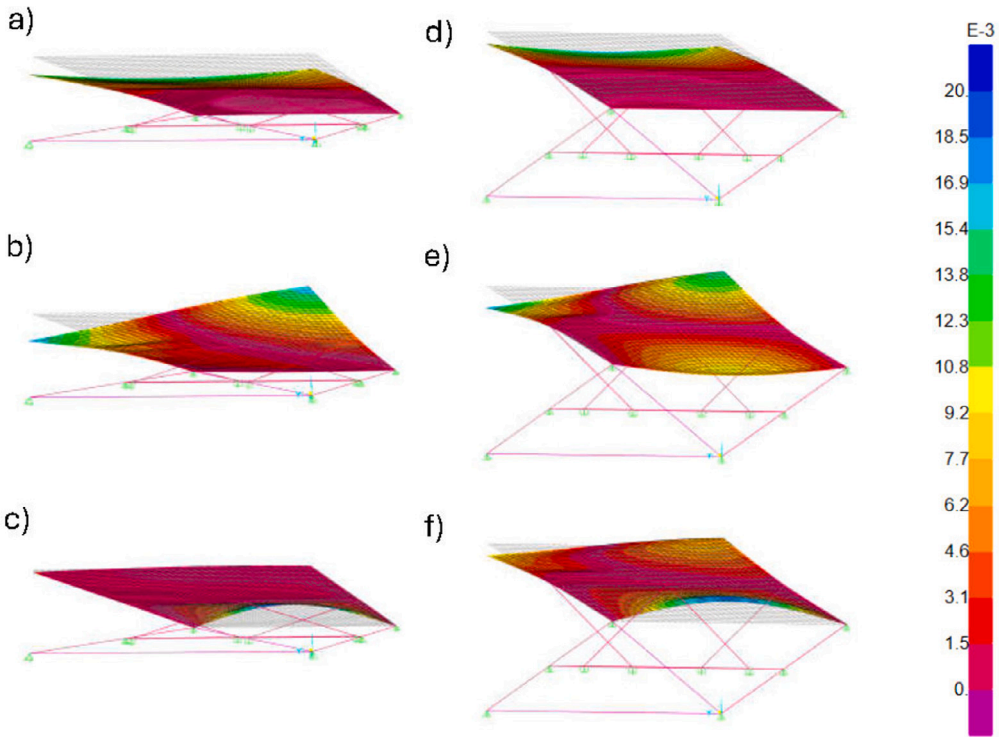

Fig. 8. Deformed shapes of the first three vibration modes of the roof module with $\hat{\theta} = 30°$ (a–c) and $\hat{\theta} = 75°$ (d–f), $\tau = 40\%$ MBF, and bus cable diameter $d = 57$ mm. The colorbar shows the norms of the displacement vectors for the mode shapes, normalized with respect to the mass matrix. Modal deformed shapes are plotted with a magnification factor of 100. (For interpretation of the references to color in this figure legend, the reader is referred to the web version of this article.)

Table 6
Periods (T) and frequencies (f) of the first three modes of vibrations of the roof module with $\hat{\theta} = 30°$, for different prestress levels τ [% MBF] applied to the bus cables with diameters $d = 57$ mm and $d = 66$ mm.

$\hat{\theta} = 30°$		Periods T [s]		Frequencies f [Hz]	
Mode	τ [%]	$d = 57$ mm	$d = 66$ mm	$d = 57$ mm	$d = 66$ mm
1	0	0.656	0.607	1.525	1.647
2	0	0.320	0.304	3.127	3.286
3	0	0.242	0.238	4.124	4.204
1	25	0.646	0.517	1.548	1.934
2	25	0.315	0.300	3.176	3.337
3	25	0.243	0.233	4.116	4.292
1	40	0.530	0.517	1.889	1.934
2	40	0.313	0.300	3.197	3.337
3	40	0.233	0.233	4.285	4.292

Table 7
Periods (T) and frequencies (f) of the first three modes of vibrations of the roof module with $\hat{\theta} = 45°$.

$\hat{\theta} = 45°$		Periods T [s]		Frequencies f [Hz]	
Mode	τ [%]	$d = 57$ mm	$d = 66$ mm	$d = 57$ mm	$d = 66$ mm
1	0	0.530	0.511	1.888	1.956
2	0	0.270	0.264	3.709	3.795
3	0	0.234	0.233	4.267	4.283
1	25	0.489	0.482	2.046	2.077
2	25	0.269	0.263	3.721	3.803
3	25	0.232	0.232	4.303	4.311
1	40	0.489	0.482	2.047	2.077
2	40	0.269	0.263	3.721	3.803
3	40	0.232	0.232	4.303	4.311

frequencies below approximately 1 Hz (see, e.g., Holmes and Bekele (2021), Ch. 5). The results of the present study indicate fundamental frequencies at or above nearly 2 Hz for the pretensioned configurations, thereby meeting the 1 Hz threshold with a comfortable safety margin. Accordingly, under these conditions, wind effects may reasonably be treated as quasi-static in preliminary assessments.

6. Solar energy harvesting capacity

This section estimates the solar energy harvesting potential of a soccer stadium incorporating the deployable roof modules introduced earlier. Specifically, we examine a redesign of the 'TWS' stadium analyzed in Nazifi Charandabi et al. (2025), which consisted of four separate grandstand sections forming the edges of a rectangular, four-pitched solar roof (cf. Fig. 2). In contrast, the stadium analyzed in the present work features a roof arranged along a Lamé superellipse (Gielis, 2003), which is mathematically described by the following equation

$$\left|\frac{x}{a}\right|^n + \left|\frac{y}{b}\right|^n = 1. \tag{14}$$

Here, n is a positive real number; x and y are the coordinates of a Cartesian reference frame whose z-axis is orthogonal to the soccer field and whose origin is located at the center of the field; and a and b are the lengths of the semi-axes of the superellipse. To obtain a shape comparable to that of the TWS stadium, we hereafter focus on the case $n = 6$, which generates a nearly rectangular shape (see Fig. 9). This configuration allows for a convenient and flexible orientation of the PV modules mounted on the roof, as will be discussed in the sequel.

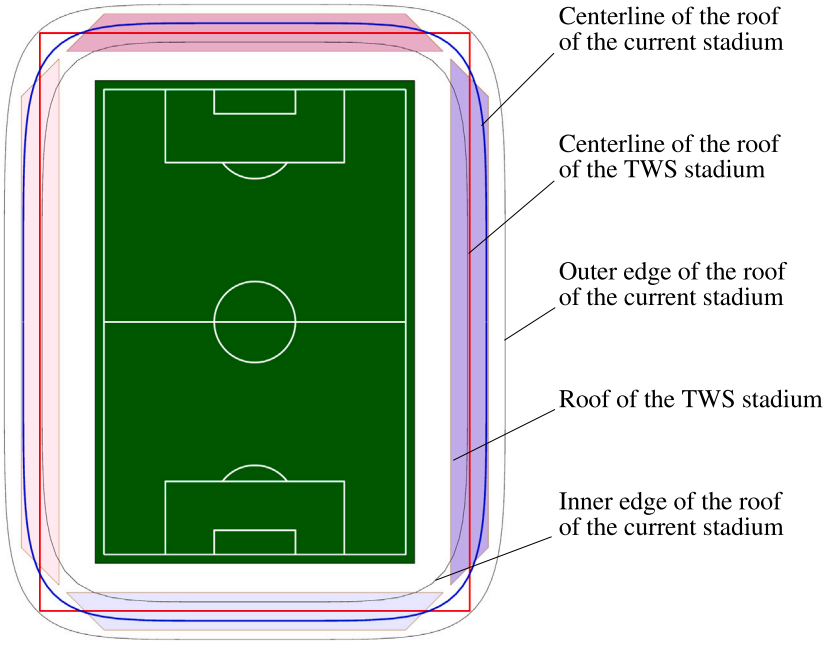

Fig. 9. Comparison of the roof profiles of the TWS stadium (red) and the current stadium (blue). (For interpretation of the references to color in this figure legend, the reader is referred to the web version of this article.)

Table 8
Periods (T) and frequencies (f) of the first three modes of vibrations of the roof module with $\hat{\theta} = 75°$.

$\hat{\theta} = 75°$		Periods T [s]		Frequencies f [Hz]	
Mode	τ [%]	$d = 57$ mm	$d = 66$ mm	$d = 57$ mm	$d = 66$ mm
1	0	0.473	0.468	2.115	2.135
2	0	0.248	0.247	4.025	4.046
3	0	0.233	0.233	4.287	4.298
1	25	0.465	0.463	2.150	2.162
2	25	0.248	0.247	4.025	4.045
3	25	0.233	0.232	4.301	4.311
1	40	0.465	0.463	2.150	2.162
2	40	0.248	0.247	4.025	4.045
3	40	0.233	0.232	4.301	4.311

We assume that the length of the inner edge of the roof of the current stadium is equal to 24 L, where $L = 16.97$ m is the length of the frontal edge of a generic deployable solar module mounted on the roof structure (see Fig. 3). In addition, we assume that the area enclosed by the centerline of the roof in the x–y plane is equal to that enclosed by the corresponding centerline of the TWS stadium. Finally, we adopt a roof module width of $D = 13.00$ m, as shown in Fig. 6. These assumptions allow us to mount 24 deployable solar modules on the roof and lead to the following dimensions of the superellipses defining the profiles of the current stadium ($a_c = 51.812$ m, $b_c = 66.989$ m) for the centerline; ($a_i = 48.023$ m, $b_i = 63.345$ m) for the inner edge; and ($a_o = 55.601$ m, $b_o = 70.633$ m) for the outer edge of the roof. The overall surface area of the 24 roof modules is equal to 4011.38 m^2 (with each module having a surface area of 167.141 m^2). We estimate that the total illuminated area of the PV panels is 90% of the total roof area, i.e., approximately 3610.24 m^2, following a similar assumption made in Nazifi Charandabi et al. (2025). Fig. 10, generated using Rhinoceros® CAD software, presents two views of the current solar stadium roof, which is mounted on a supporting steel structure replicating that of the TWS stadium. It is worth emphasizing once again that the current deployable solar roof can be adapted to vertical structures of any architectural design.

Our current goal is to optimize the secondary tilting angles $\hat{\theta}$ of the 24 roof modules forming the current stadium, over the course of the entire year 2023 at the Salerno site. We assume that the roof has a reference configuration featuring an initial tilting angle of $\theta_0 = 30.509°$ about the frontal edge, as in the previous sections, and that the secondary tilting angles $\hat{\theta}$ of the roof modules can range from 0° to $\hat{\theta}_{\max} = 119°$, as in the case of the TWS stadium (see Section 4) The optimal values of these tilting angles are computed using the algorithm thoroughly described in Nazifi Charandabi et al. (2025) and Babilio (2025), which is briefly summarized here. At any instant t of a given day, the total solar input power P_{in} on the stadium roof can be estimated as

$$P_{in}(t) = \sum_{m=1}^{N} I_{b,n}(t)\, A_b^m\, \boldsymbol{n}_s(t) \cdot \boldsymbol{n}_m(\hat{\theta}^m(t))\,, \tag{15}$$

where $I_{b,n}$ denotes the direct normal irradiance (DNI), $\hat{\theta}^m$ is the secondary tilting angle of mth roof module, A_b^m is the direct-beam-illuminated area of such a module, $\boldsymbol{n}_m$ is the normal vector to the module, $N = 24$ is the total number of modules, $\boldsymbol{n}_s$ is the unit vector in the direction of the sun rays and the dot $(\cdot)$ stands for the scalar products between vectors. The adopted PV panels are assumed to be monofacial. For the sake of simplicity, both the diffuse horizontal irradiance and the ground-reflected components of the global solar irradiance are neglected (Gao et al., 2018). Shadowing effects due to cloud cover, irradiance attenuation caused by the accumulation of dirt or other materials on the panel surfaces, and mutual shading between adjacent roof modules are also disregarded. The latter simplification is justified by the expectation that the tilting angles of the PV modules vary smoothly along the roof span, and by the fact that several modules are sufficiently spaced along the outer edge of the roof (see Fig. 10). The optimal tilting angles $\hat{\theta}^m$ are obtained through a sun-tracking procedure that maximizes P_{in} at discrete time instances within the time window from sunrise to sunset, using the `NMaximize` function in *Mathematica*® (Nazifi Charandabi et al., 2025) and solar data provided by PVLib v0.10.3 (Holmgren et al., 2018).

The study is conducted with reference to twelve representative days in 2023, selecting one day per month, consistent with the approach adopted for the TWS stadium. The chosen dates include March 20 and September 23 (spring and autumn equinoxes), June 21 and December 21 (summer and winter solstices), and the 15th day of each of the remaining months. Fig. 11a shows the reference configuration of the

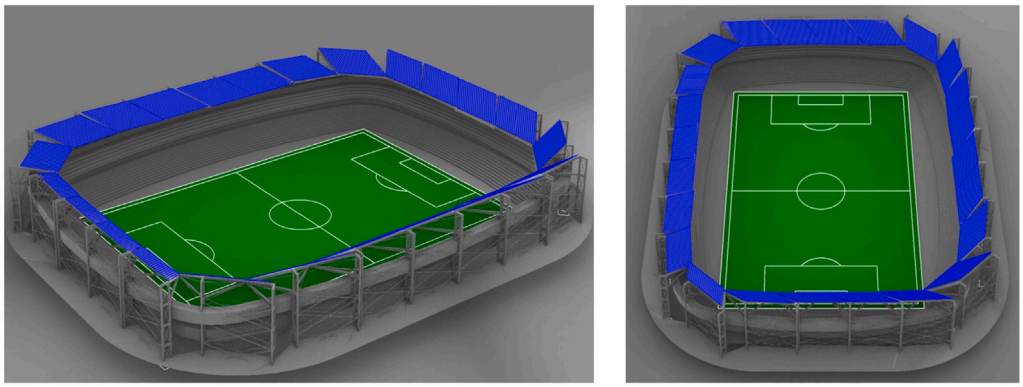

Fig. 10. Different perspectives of a sports stadium equipped with the current solar roof modules.

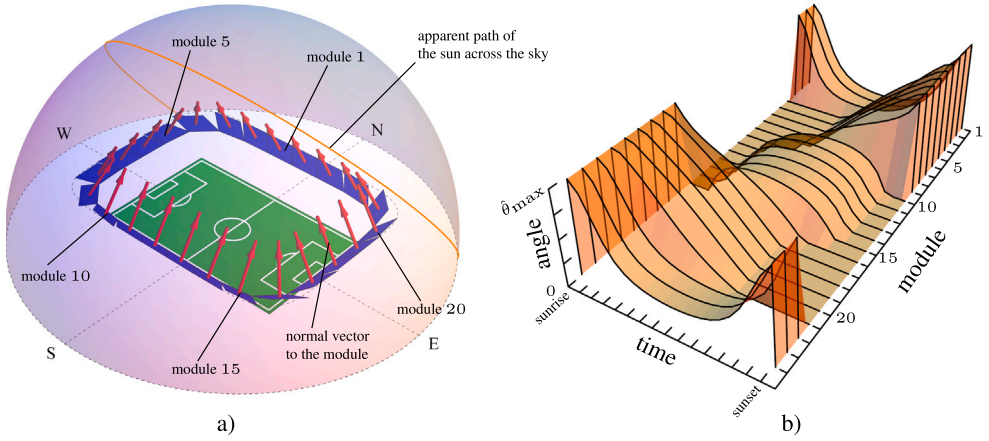

Fig. 11. (a) Illustration of the reference configuration of the current stadium. (b) Plot showing the optimal values of the secondary tilting angles obtained for each roof module during the summer solstice of 2023 at the Salerno site.

current stadium, while Fig. 11b illustrates the time variation of the optimal secondary tilting angles of the roof modules over the course of the summer solstice of 2023 at the Salerno site. The solar input energy in a given day is obtained as

$$E_{in} = \int_{t_{sr}}^{t_{ss}} P_{in}(t)\,\mathrm{d}t\,, \tag{16}$$

where t_{sr} and t_{ss} represent the sunrise and sunset times of the day, respectively. Multiplying E_{in} by the number of days in each month provides a rough estimate of the monthly input energy. The yearly input energy is then obtained by summing the twelve monthly values. A graphical comparison of the monthly input energy (in MW h) for the TWS stadium and the current stadium is presented in Fig. 12.

The results in Fig. 12 illustrate that the current stadium design yields a significant increase in solar input energy over the entire year. It is worth noting that the sun-tracking strategy adopted for the current stadium allows each of the 24 roof modules to tilt independently, whereas the strategy used for the TWS stadium assumes a constant tilting angle for each of the four grandstands forming the roof. Additionally, the solar roof modules designed for the current stadium can be readily generalized and adapted to an existing stadium of arbitrary geometry, whereas those analyzed in Nazifi Charandabi et al. (2025) are fully integrated into the supporting structure. Let us estimate the percentage increase in the monthly solar input energy when transitioning from the TWS stadium to the current stadium, using the following equation

$$\iota = 100\,\frac{E_{in}^{\mathrm{CUR}} - E_{in}^{\mathrm{TWS}}}{E_{in}^{\mathrm{TWS}}}\,, \tag{17}$$

where E_{in}^{CUR} denotes the input solar energy for the current stadium in a given month, while E_{in}^{TWS} denotes the corresponding energy value for the TWS stadium. Fig. 12 shows that the minimum and maximum energy gains ι are obtained in July (+11.75%) and December (+18.64%), respectively. It is worth noting that E_{in}^{CUR} reaches 845.64 MW h in July and 496.33 MW h in December. The yearly input solar energy amounts to 8397.18 MW h for the current stadium, compared to 7411.94 MW h for the TWS stadium, corresponding to a percentage increase of +13.29%.

Assuming a power conversion efficiency (PCE) of $\eta = 24\%$ for the PV cells used in the SunBender S47 panels (Solbian, 2025), we estimate a yearly electrical energy output E_{out} of approximately 2015 MW h for the current solar stadium, compared to 1771 MW h for the TWS stadium, under the same PCE assumption (Nazifi Charandabi et al., 2025). The optimal tilting angles obtained for the various roof modules of the current stadium during the summer solstice are shown in Fig. 13 at selected times, with UTC denoting Coordinated Universal Time (see also the animation provided in the Supplementary Material). We close by analyzing the peak input power values $\hat{P}_{in}$ estimated using the current sun-tracking procedure, which are listed in Table 9 for the representative days of the reference year. It is observed that the absolute maximum of $\hat{P}_{in}$ occurs in June and is nearly equal to 3081 kW. For a power conversion efficiency of $\eta = 24\%$, this corresponds to a peak output power of $\hat{P}_{out} \approx 740$ kW. A suitable power management strategy for the PV modules can be implemented to maximize energy production, accounting for inherent mismatches among the roof modules due to varying tilt and azimuth angles under the adopted sun-tracking strategy, as well as partial shading, uneven dust deposition, and similar effects. The use of microinverters and power optimizers enables distributed Maximum Power Point Tracking (MPPT) across

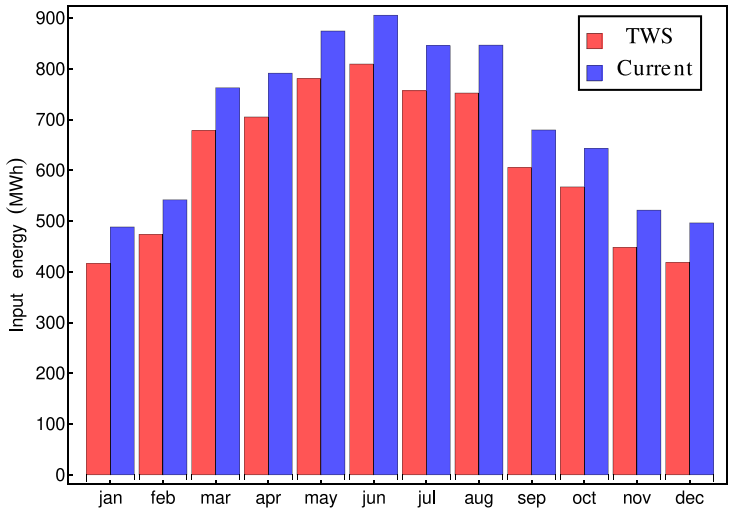

Fig. 12. Comparison of the monthly input energy values numerically estimated for the current stadium and the TWS stadium.

Table 9
Peak input solar power values for the current stadium on selected days of each month in the reference year.

Month	Peak time (UTC+1)	Peak input power (kW)
Jan	12:13	2215.907
Feb	12:15	2539.532
Mar	12:09	2949.104
Apr	12:58	3010.686
May	12:50	3023.872
Jun	13:05	3081.449
Jul	13:02	2913.506
Aug	13:09	3012.092
Sep	12:54	2779.256
Oct	12:46	2645.016
Nov	11:52	2357.087
Dec	11:56	2237.963

the multiple roof modules, thereby minimizing mismatch losses and facilitating operation and maintenance to ensure long-term PV plant performance and timely repair actions. The system is designed for direct integration of the solar power into the stadium's electrical grid, allowing the harvested energy to be either self-consumed within the facility (e.g., lighting, heating, ventilation, and air conditioning, and other services) or exported to the local grid, depending on demand and regulatory frameworks (Gao et al., 2018; International Energy Agency, 2023).

7. Concluding remarks

This work has presented an innovative reformulation of a deployable roof concept for solar sports stadiums, recently introduced in the literature, which enables the easy integration of a tiltable tensegrity system with a wide range of existing or new roof structures. The main innovation of the tensegrity design proposed in this study lies in the use of a mechanism based on sliding supports connected to deployment-actuating struts. This system can be readily integrated onto any flat roof, whether horizontal or inclined (see Sections 2–3), whereas the tensegrity system employed in the TWS stadium is constrained by the specific supporting structure of that stadium. We observe that the majority of solar roofs for sports stadiums proposed and built to date do not incorporate photovoltaic panels with sun-tracking capabilities (see, for instance, the notable examples in Ahshan et al. (2020), Manni et al. (2018), Architectuul (2013) and Euronews (2022), as well as the reviews in Solarplaza (2018) and PowerTechnology (2019)). By contrast, the study presented in Nazifi Charandabi et al. (2025) demonstrates that implementing an appropriate sun-tracking strategy enables the optimal orientation of solar panels mounted on the roofs of a solar stadium, resulting in annual energy production increases of approximately 50% and peak power gains of up to 80% during the winter months.

The mechanical analysis presented in Sections 4–5 demonstrates that the proposed deployable roof system can safely withstand wind forces under a simplified quasi-static wind loading model, provided that the tensegrity members are properly dimensioned, the bus cable is adequately pretensioned, and the photovoltaic panels exhibit sufficient flexibility. This study represents another significant advancement over the work presented in Nazifi Charandabi et al. (2025), which investigated the mechanical response of a tensegrity roof for a sports stadium only in the undeployed configuration. Optimal functioning of the proposed sun-tracking roof system can be achieved by equipping it with anemometer sensors to monitor wind speed and automatically trigger the untilting of the modules under high wind conditions, particularly in configurations characterized by low tilting angles $\hat{\theta}$. Such conditions may potentially give rise to dynamic effects and resonance-type responses in the system under severe weather conditions. It is worth noting, however, that potential resonant responses of the deployable roof panels, where necessary, can be investigated by adapting existing methodologies originally developed for large-span roofs (Su et al., 2018) and photovoltaic modules (Wittwer et al., 2022), accounting for the available level of aerodynamic or structural damping (Holmes and Bekele, 2021).

The deployable roof system analyzed in this study leverages a sun-tracking strategy that incorporates a winch mechanism proven to operate with reduced energy input (Fraternali et al., 2024a). In Section 6, we presented a study on the implementation of a flexible sun-tracking strategy for a solar stadium equipped with deployable roof modules. This approach assigns distinct tilting angles to different portions of the structure and, as demonstrated through an illustrative example, has been shown to yield significant increases in electric power production. We estimated an increase of approximately 13% in both the yearly input solar energy and the output electrical energy for the current stadium compared to the reference TWS stadium, with monthly increases ranging from about 12% in July to 19% in December of the reference year. It should be noted that the solar energy harvesting capacity of the TWS stadium was already found to be significantly higher than that of a fixed-slope solar roof, as previously observed. Based on the data provided in Nazifi Charandabi et al. (2025), the gain in yearly produced electrical energy for the current small-to-medium-scale solar stadium (with a seating capacity of approximately 10 000

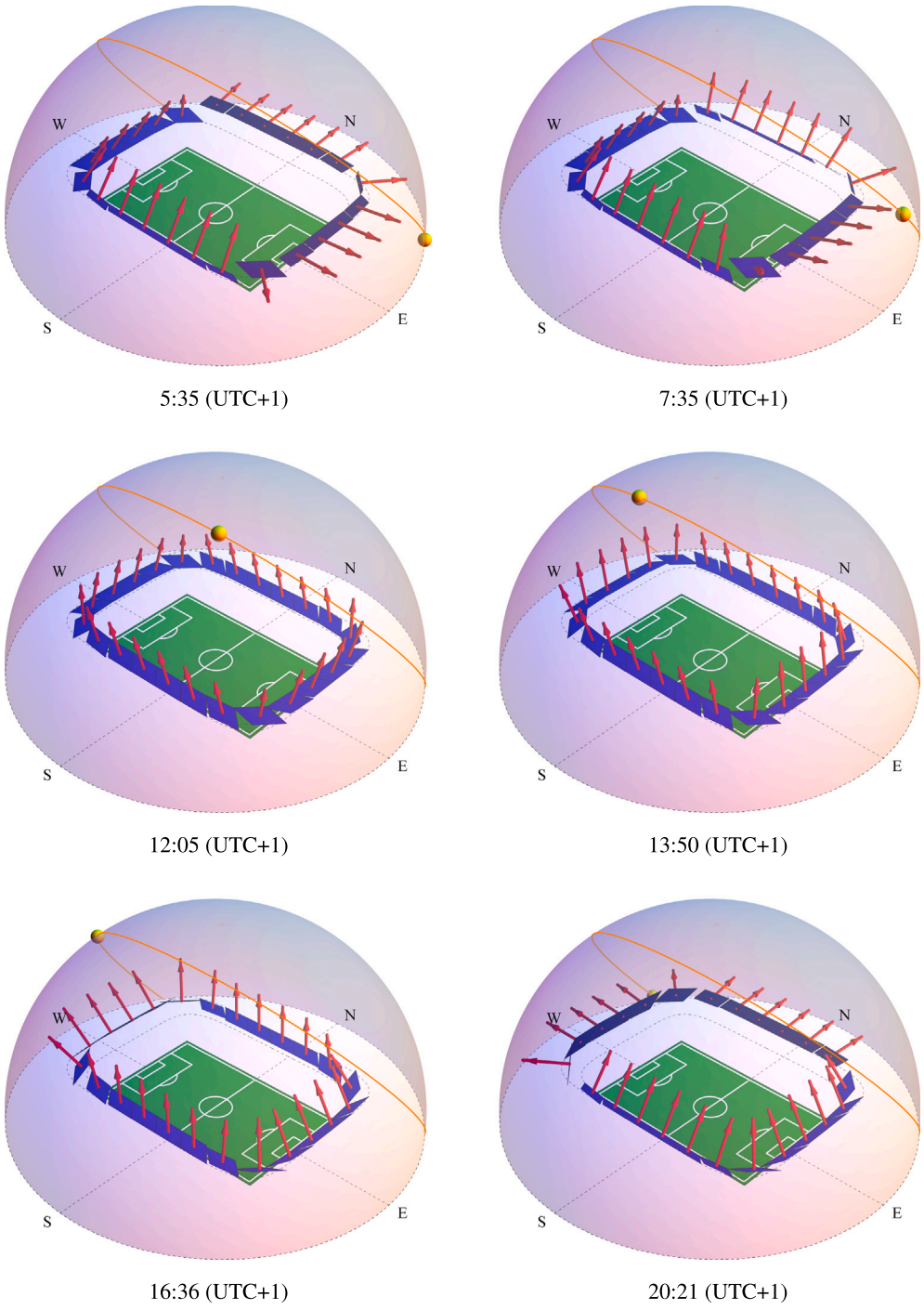

Fig. 13. Optimal configurations of the deployable roof modules forming the current stadium at different times during the summer solstice of the reference year (2023) at the Salerno site.

seats), relative to an equal-sized fixed-slope roof equipped with the same type of PV panels, is estimated to be approximately 75%. In addition, we note that the peak output power of the current stadium is approximately 740 kW. This value is notably high, corresponding to about 74% of the peak output power generated by the significantly larger Bentegodi Stadium in Verona, Italy (1000 kW), which has nearly four times the seating capacity of the current stadium (Solarplaza, 2018).

Overall, we conclude that the deployable roof system analyzed in the present study shows strong potential both for the design of novel sports stadiums equipped with efficient sun-tracking strategies and for the retrofit of existing stadiums aimed at enhancing their energy performance. We intend to extend this research through future work focused on the fabrication and testing of physical mockups, which will be subjected to both static testing (Feron et al., 2023) and dynamic testing in a wind tunnel (Brusco et al., 2024; Taylor et al., 2024). In parallel, we plan to investigate the benefits and challenges of both retrofitting existing sports stadiums and designing new ones with the proposed solar roof modules, by varying their geometries and the overall stadium architecture (Safarpour et al., 2025). Additional lines

of research will explore the integration of bifacial PV cells on dynamic stadium roofs, enabling the harvesting of diffuse and ground-reflected solar radiation. Furthermore, Return on Investment (ROI) analyses will be carried out to assess the economic viability of deployable solar roof systems in sports stadiums.

CRediT authorship contribution statement

Rana Nazifi Charandabi: Writing – review & editing, Writing – original draft, Visualization, Validation, Supervision, Software, Methodology, Investigation, Formal analysis, Data curation, Conceptualization. **Julia de Castro Motta:** Writing – review & editing, Writing – original draft, Methodology, Investigation, Funding acquisition, Formal analysis, Data curation, Conceptualization. **Gerardo Carpentieri:** Writing – review & editing, Writing – original draft, Visualization, Validation, Supervision, Software, Methodology, Investigation, Formal analysis, Data curation, Conceptualization. **Enrico Babilio:** Writing – review & editing, Writing – original draft, Visualization, Validation, Supervision, Software, Methodology, Investigation, Funding acquisition, Formal analysis, Data curation, Conceptualization. **Jordi Bonada:** Writing – review & editing, Writing – original draft, Visualization, Validation, Data curation, Conceptualization. **Nicholas Fantuzzi:** Writing – review & editing, Writing – original draft, Visualization, Validation, Formal analysis, Conceptualization. **Fernando Fraternali:** Writing – review & editing, Writing – original draft, Visualization, Validation, Supervision, Software, Resources, Project administration, Methodology, Investigation, Funding acquisition, Formal analysis, Data curation, Conceptualization.

Funding

This work was supported by the National Recovery and Resilience Plan (NRRP), Mission 4, Component 2, Investment 1.1, Call for tender No. 104 published on 2.2.2022 by the Italian Ministry of University and Research (MUR), funded by the European Union – NextGenerationEU – Project Titles 'The mathematics and mechanics of nonlinear wave propagation in solids (MMWS) – 2022P5R22A – CUP D53D23003890006 (JdCM); 'Innovative tensegrity lattices and architectured metamaterials' (ILAM) – 20224LBXMZ – CUP D53D23003020006 (FF); - Grants Assignment Decree No. 961 adopted on 30.6.2023 by the Italian Ministry of University and Research (MUR). It has also been supported by the National Recovery and Resilience Plan (NRRP), Mission 4, Component 2, Investment 1.1, Call for tender No 1409 published on 14.9.2022 by the Italian Ministry of University and Research (MUR), funded by the European Union – NextGenerationEU – Project Titles 'Sustainable composite structures for energy harvesting and carbon-storing buildings' (SUSTBUILD) – P2022PE8BT – CUP D53D23018440001 (FF); 'Stabilization of contaminated soils' (STABSOIL) – P2022CR8AJ – CUP D53D23018180001 (FF); 'A fluid–structure interaction tool for the protection of clean energy production sites' (FSI-CEP) – P20227CSJ5 – CUP E53D23016930001 (EB) – Grants Assignment Decree No. 1385 adopted on 1.9.2023 by the Italian Ministry of University and Research (MUR). FF also acknowledges support by the Italian Ministry of Foreign Affairs and International Cooperation within the Italy-USA Science and Technology Cooperation Program 2023–2025, Project 'Next-generation green structures for natural disaster-proof buildings', grant number US23GR15. EB thanks the Italian National Group for the Mathematical Physics (GNFM) of the National Institute for Advanced Mathematics (INdAM). RNC thanks the Italian Dottorato di Interesse Nazionale 'Photovoltaics'.

Declaration of competing interest

The authors declare that they have no known competing financial interests or personal relationships that could have appeared to influence the work reported in this paper.

Appendix A. Supplementary data

A movie illustrating the sun-tracking strategy of the current stadium design during the summer solstice of the reference year is provided as Supplementary Material.

Supplementary material related to this article can be found online at https://doi.org/10.1016/j.dibe.2025.100771.

Data availability

Data will be made available on request.

References

Ahshan, R., Al-Abri, R., Al-Zakwani, H., Ambu-Saidi, N., Hossain, E., 2020. Design and economic analysis of a solar photovoltaic system for a campus sports complex. Int. J. Renew. Energy Res. (IJRER) 10 (1), 67–78.

Architectuul, 2013. Kaohsiung Stadium. (Accessed: August 12 2025) https://architectuul.com/architecture/kaohsiung-stadium.

Babilio, E., 2025. Mathematica Notobook for the article 'A tensegrity structure for a solar stadium roof with sun-tracking capability'. (Accessed: August 12 2025) https://community.wolfram.com/groups/-/m/t/3396614.

Bellini, E., 2025. Sun-tracking photovoltaics for stadiums. (Accessed: August 12 2025) https://www.pv-magazine.com/2025/03/03/sun-tracking-photovoltaics-for-stadiums/.

Born, L., Martin, E.A.G.S., Ridder, M., Koerner, A.H., Knippers, J., Gresser, G.T., 2024. FlectoSol-a pneumatically activable PV-functionalized facade shading module with bending motion in two directions for solar tracking. Dev. the Built Environ. 18.

Brusco, S., Bin, H.-Y., Lo, Y.-L., Piccardo, G., 2024. Transient aerodynamics of a square cylinder under downburst-like accelerating flows reproduced in a multiple-fan wind tunnel. J. Fluids Struct. 124, 104038.

Cheggaga, N., Dahli, K., Hammouda, M.R., Benallal, A., Ilinca, A., 2024. Innovative shade mitigation technique for maximizing solar energy efficiency in roof-mounted PV systems. J. Eur. Des Syst. Automatisés 57 (4), 1155–1164.

Computers and Structures, Inc., 2016. SAP2000: Integrated Finite Element Analysis and Design of Structures. Computers and Structures, URL: https://docs.csiamerica.com/manuals/sap2000/CSiRefer.pdf.

Euronews, 2022. Green Galatasaray: Turkish football giant saves almost €400,000 from its solar roof. (Accessed: August 12 2025) https://www.euronews.com/green/2022/10/03/green-galatasaray-turkish-.

European Committee for Standardization (CEN), 2024. EN 1993-1-1:2022 Eurocode 3: Design of Steel Structures - Part 1-8: Design of joints . European Standard.

Feron, J., Rhode-Barbarigos, L., Latteur, P., 2023. Experimental testing of a tensegrity simplex: self-stress implementation and static loading. J. Struct. Eng. 149 (7), 04023073.

Fondazione Promozione Acciaio, 2024. Profilati cavi per usi strutturali (in Italian). (Accessed: August 12 2025) https://www.promozioneacciaio.it/UserFiles/File/pdf/pubblicazioni/03_profilicavi.pdf.

Fraternali, F., Babilio, E., Nazifi Charandabi, R., Germano, G., Luciano, R., Spagnuolo, G., 2024a. Dynamic origami solar eyes with tensegrity architecture for energy harvesting Mashrabiyas. Appl. Eng. Sci. 19, 100190.

Fraternali, F., de Castro Motta, J., Germano, G., Babilio, E., Amendola, A., 2024b. Mechanical response of tensegrity-origami solar modules. Appl. Eng. Sci. 17, 100174.

Gao, Y., Dong, J., Isabella, O., Santbergen, R., Tan, H., Zeman, M., Zhang, G., 2018. A photovoltaic window with sun-tracking shading elements towards maximum power generation and non-glare daylighting. Appl. Energy 228, 1454–1472.

Gao, Y., Dong, J., Isabella, O., Santbergen, R., Tan, H., Zeman, M., Zhang, G., 2019. Modeling and analyses of energy performances of photovoltaic greenhouses with sun-tracking functionality. Appl. Energy 233, 424–442.

Gielis, J., 2003. Inventing the Circle: the Geometry of Nature. Geniaal Press, The Netherlands, ISBN: 978-90-807756-1-9.

Heinzelmann, F., 2018. Design Method for Adaptive Daylight Systems for Buildings Covered by Large (Span) Roofs (Ph.D. thesis). Technische Universiteit Eindhoven.

Holmes, J.D., Bekele, S.A., 2021. Wind Loading of Structures: Fourth Edition. CRC Press.

Holmgren, W.F., Hansen, C.W., Mikofski, M.A., 2018. Pvlib python: A python package for modeling solar energy systems. J. Open Source Softw. 3 (29), 884.

International Energy Agency, 2023. Renewables 2023: Analysis and forecast to 2028. URL: https://www.iea.org/reports/renewables-2023 (Accessed: September 14, 2025).

Lim, B.-H., Lim, C.-S., Li, H., Hu, X.-L., Chong, K.-K., Zong, J.-L., Kang, K., Tan, W.-C., 2020. Industrial design and implementation of a large-scale dual-axis sun tracker with a vertical-axis-rotating-platform and multiple-row-elevation structures. Sol. Energy 199, 596–616.

Manni, M., Coccia, V., Nicolini, A., Marseglia, G., Petrozzi, A., 2018. Towards zero energy stadiums: The case study of the Dacia Arena in Udine, Italy. Energies 11 (9), 2396.

Nazifi Charandabi, R., Babilio, E., Carpentieri, G., Spagnuolo, G., Amendola, A., Fraternali, F., 2025. A tensegrity structure for a solar stadium roof with sun-tracking capability. Thin-Walled Struct. 113033.

NTC, 2018. D.M. 17/01/2018. Norme Tecniche per le Costruzioni (in Italian). Gazz. Uff. N. 42 Del 20/02/2018, Suppl. Ordin. N.8 42.

Pawlak-Jakubowska, A., 2023. Retractable roof module with photovoltaic panel as small solar power plant. Energy Build. 288, 112994.

PowerTechnology, 2019. Renewable stadiums of the future. (Accessed: August 12 2025) https://www.power-technology.com/features/best-stadiums-renewable-energy/.

Safarpour, A., Laleh, S.S., Soltani, S., 2025. Identifying challenges, benefits, and recommendations for utilizing solar panels in sport stadiums: A thematic analysis. Prog. Eng. Sci. 2 (1), 100035.

Sirtef srl, 2025. Structural Spiral Strands. (Accessed: August 12 2025) https://www.sirtef.it/en/products/steel-wire-ropes/spiral-strands-structural-spiral-strands/.

Solarplaza, 2018. Top 50 Solar Stadiums Worldwide (2018 World Cup Edition). (Accessed: August 12 2025) https://www.solarplaza.com/resource/11879/top-50-solar-.

Solbian, 2025. SunBender solar panels. (Accessed: August 12 2025) https://blog.solbian.eu/en/sunbender.

Solbian Manual, 2025. Solbian Solar Panel User's Manual . (Accessed: August 12 2025) https://www.emarineinc.com/Shared/pdf/Solbian/Solbian-Users-Manual.pdf.

Su, N., Peng, S., Hong, N., 2018. Analyzing the background and resonant effects of wind-induced responses on large-span roofs. J. Wind Eng. Ind. Aerodyn. (ISSN: 0167-6105) 183, 114–126.

Tahmasebinia, F., Chen, E., Huang, A., Li, J., 2023. Designing lightweight stadium roofing structures based on advanced analysis methods. Sustainability 15 (4), 3612.

Taylor, Z.J., Feero, M.A., Browne, M.T., 2024. Aeroelastic instability mechanisms of single-axis solar trackers. J. Wind Eng. Ind. Aerodyn. 244, 105626.

Ürge-Vorsatz, D., Chatterjee, S., Cabeza, L.F., Molnár, G., 2025. Global and regional estimation and evaluation of suitable roof area for solar and green roof applications. Dev. the Built Environ. 21, 100607.

Wittwer, A.R., Podestá, J.M., Castro, H.G., Mroginski, J.L., Marighetti, J.O., De Bortoli, M.E., Paz, R.R., Mateo, F., 2022. Wind loading and its effects on photovoltaic modules: An experimental–computational study to assess the stress on structures. Sol. Energy 240, 315–328.